Decontamination of Radionuclides from Concrete by Microwave Heating. II: Computations

Goangseup Zi[1] and Zdeněk P. Bažant, F.ASCE[2]

Abstract: Based on a mathematical model developed in the preceding Part I of this study, a numerical analysis of the process of decontamination of radionuclides from concrete by microwave heating is conducted. The aim is to determine the required microwave power and predict whether and when the contaminated surface layer of concrete spalls off. As customary, the finite element method is used for the stress and fracture analysis. However, as a departure from previous studies, the finite volume method is adopted to treat the heat and moisture transfer, in order to prevent spurious numerical oscillations that plagued the finite element response at moving sharp interface between the saturated and unsaturated concrete, and to deal accurately with the jumps in permeability and in sorption isotherm slope across the interface. The effects of wall thickness, reinforcing bars, microwave frequency, and power are studied numerically. As a byproduct of this analysis, the mechanism of spalling of rapidly heated concrete is clarified.

DOI: 10.1061/(ASCE)0733-9399(2003)129:7(785)

CE Database subject headings: Computation; Concrete; Microwaves; Contamination; Contaminants; Heating; Diffusion; Thermal stresses; Pore pressure.

Introduction

Based on the model developed in the preceding Part I of this study (Bažant and Zi 2003), we will now conduct numerical analysis of the evolution of the fields of temperature, pore pressure, and stress during rapid microwave heating and analyze the implications for the process of radionuclide decontamination of concrete. For stress and deformation analysis, we will employ the finite element method [Fig. 1(b)]. On the other hand, for the heat and moisture transfer, we will adopt the finite volume method [Fig. 1(a)], which will be a departure from the previous practice in nuclear reactor safety research and fire research (Bažant and Thonguthai 1978, 1979; Bažant and Kaplan 1996; Ahmed and Hurst 1997). Thanks to enforcing exactly the local mass and heat conservation even though the water and heat fluxes are only approximate, this method (Patankar 1980) can suppress the spurious numerical oscillations that have previously been experienced with finite elements in rapid heating problems characterized by a sharp moving interface between saturated and unsaturated regions, associated with jumps in permeability and sorption isotherm slope across the interface (Bažant and Thonguthai 1978, 1979; Celia et al. 1990). For discretization in time, we will employ Picard's method, in which the differential equation coefficients are kept constant during each iteration process, in order to cope with the severe nonlinearity of the model. The analysis by finite volume method will be simplified as axisymmetric, which is doubtless an adequate approximation.

The material subroutine for the nonlinear triaxial stress–strain relation with strain-softening will be based on microplane model M4 recently developed at Northwestern University. The strains will be assumed to be small. To avoid using too small time steps because of numerical stability problems, we will use an implicit rather then explicit finite element formulation. On the other hand, since the calculation of the tangential stiffness matrix of the microplane model M4 is quite computationally demanding, the initial stiffness matrix will be used in an iterative solution of the system of nonlinear equilibrium equations.

Effects of Power Pattern

The power of the electromagnetic field produced by a point source placed in a free space (having no dielectric loss) decays in space in proportion to r^{-2}, where r = distance between the source and a point where the power is measured. This decay is reflected in the Poynting vector (e.g., Cheng 1983). The power decay in space is affected by the composition of the medium, the type of antenna and other factors.

The effects of various power patterns must be solved from the Maxwell equations [see Eqs. (2*a*) and (2*b*) in Part I]. Both the applicator (antenna) (Fig. 1 in Part I) and concrete need, in general, to be included in the analysis of electromagnetic wave propagation. The power may be approximately considered to flow within a cone (called the solid angle) of a certain constant slope k (Kraus 1988). The effective power flux reduction due to the spreading of the cross section of this cone with distance s from the applicator may be approximated by the ratio

$$f(x)=y_0^2/(y_0+kx)^2 \tag{1}$$

where y_0 = equivalent radius of the applicator at $x=0$. Taking $y_0=6$ cm and $k\approx 0.5$, one finds the power reduction due to cross

[1]Research Associate, Dept. of Civil Engineering, Northwestern Univ., 2145 Sheridan Rd., Evanston, IL 60208. E-mail: g-zi@northwestern.edu

[2]McCormick School Professor and W. P. Murphy Professor of Civil Engineering and Materials Science, Northwestern Univ., 2145 Sheridan Rd., Evanston, IL 60208. E-mail: z-bazant@northwestern.edu

Note. Associate Editor: Franz-Josef Ulm. Discussion open until December 1, 2003. Separate discussions must be submitted for individual papers. To extend the closing date by one month, a written request must be filed with the ASCE Managing Editor. The manuscript for this paper was submitted for review and possible publication on March 12, 2002; approved on October 29, 2002. This paper is part of the ***Journal of Engineering Mechanics***, Vol. 129, No. 7, July 1, 2003. ©ASCE, ISSN 0733-9399/2003/7-785–792/$18.00.

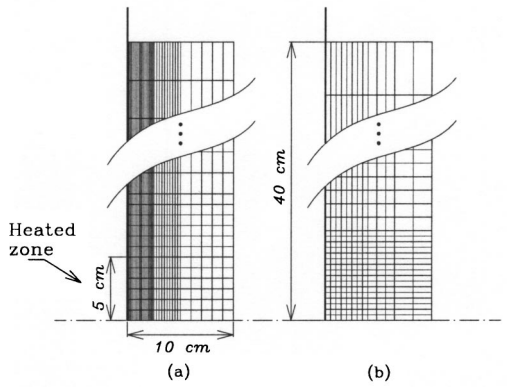

Fig. 1. (a) Finite volume mesh for analysis of heat and moisture transfer and (b) finite element mesh for analysis of mechanical deformation in which the size of one element of heated zone is set to 5 mm

section spreading to be about $f(x)=90\%$ at $x=2$ cm. But at that distance the heat generation rate for $f=18.0$ GHz is reduced to almost zero (Fig. 2). Therefore, the spreading of the effective cross section of the power flux can be neglected in practice.

Applicator Efficiency

A more important aspect of the decontamination process is the efficiency of the applicator. Obviously, the maximum efficiency is obtained for surface reflection coefficient $R_0=0$ [Eq. (5) in Part I], which means that 100% of the power input gets transmitted from the applicator into the concrete. In that case, the intrinsic impedance of the applicator, η_a, is equal to that at concrete surface, η_1. Introducing an empirical efficiency parameter $\phi \in [0,1]$, one may write

$$\eta_a=\phi\eta_1+(1-\phi)\eta_0 \tag{2}$$

where $\eta_0=$ intrinsic impedance of air. Here it is assumed that the intrinsic impedance of the applicator is in the range of $[\eta_0,\eta_1]$. The heat generation rates with the maximum efficiency (i.e., $\eta_a=\eta_1$) are plotted in Fig. 2(b) for different frequencies. For frequency $f=18.0$ GHz, the surface heat generation rate is almost

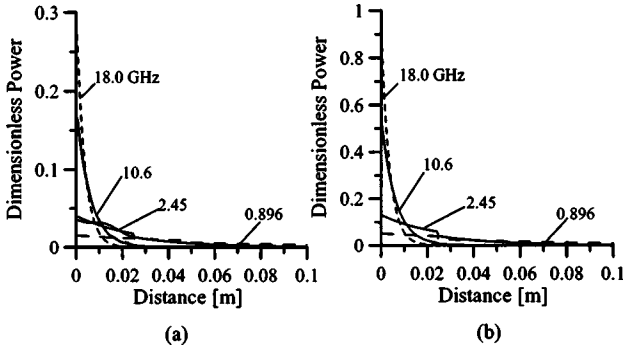

Fig. 2. Examples of volumetric heat generations calculated by Eq. (12) in Part I; (a) with zero applicator efficiency, in which heat generations for $f=2.45$,10.6 GHz are compared to heat generations averaged only in time, Eq. (11) in Part I; (b) with maximum efficiency; here, reinforcing bars are located 2.5 cm under surface to which transmission electron microscopy waves are incident

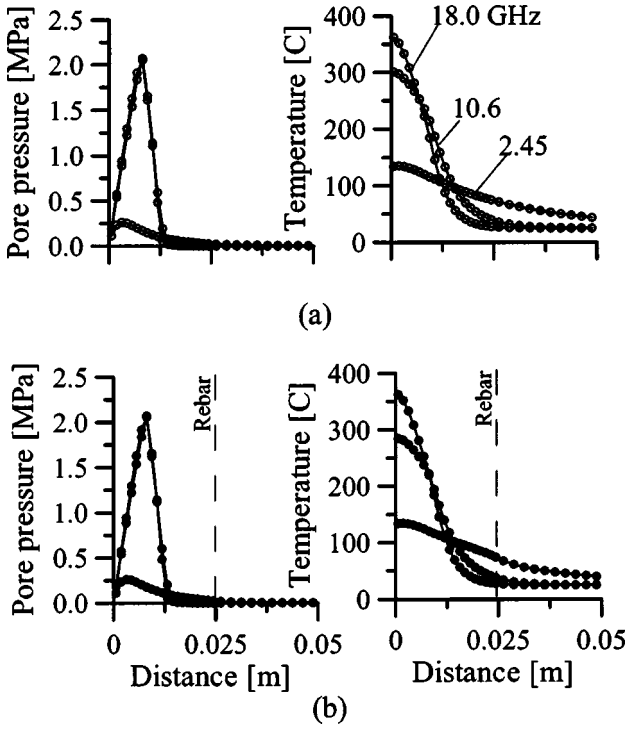

Fig. 3. Effect of reinforcing bars in 10 cm wall where 19% of reinforcing bars are located in 2.5 cm from heating surface: (a) without reinforcing bars (circles) and (b) with reinforcing bars (solid dots)

three times higher than that without any optimization [i.e., $\eta_a=\eta_0$; Fig. 2(a)]. It thus becomes clear that the efficiency ϕ of the applicator is a very important parameter, overwhelming others. Since the efficiency has not been measured experimentally, $\phi=50\%$ is assumed for the studies that follow.

Validity of Spatial Averaging of Heat Generation

The simple heat generation in Eq. (12) in Part I is obtained by means of the temporal and spatial averaging of the ohmic heat dissipation of Eq. (1) in Part I. The heat generation by temporal and spatial averaging [Eq. (12) in Part I] is compared to the heat generation by temporal averaging [Eq. (11) in Part I] in Fig. 2(a) for two frequencies: $f=2.45$ and 10.6 GHz. The former is a smooth exponential function while the latter oscillates along the radiation direction. However, the difference is negligible for $f=2.45$ and visually indistinguishable for $f=10.6$ GHz. This shows that the averaging over both space and time is justified for the practical frequency range.

Effect of Reinforcing Bars on Pore Pressures and Temperatures

As mentioned in Part I (Bažant and Zi 2003), the power carried by microwaves gets reflected from conductive materials, such as the steel reinforcing bars. To investigate this effect, the temperature and pore pressure profiles after 10 s of heating that are obtained in the absence of steel bars [Fig. 3(a)] are compared to the profiles with reinforcing bars [Fig. 3(b)] for three different microwave frequencies, $f=2.45$, 10.6, and 18.0 GHz, after 10 s of heating. The area fraction of the steel bars (in a projection on the

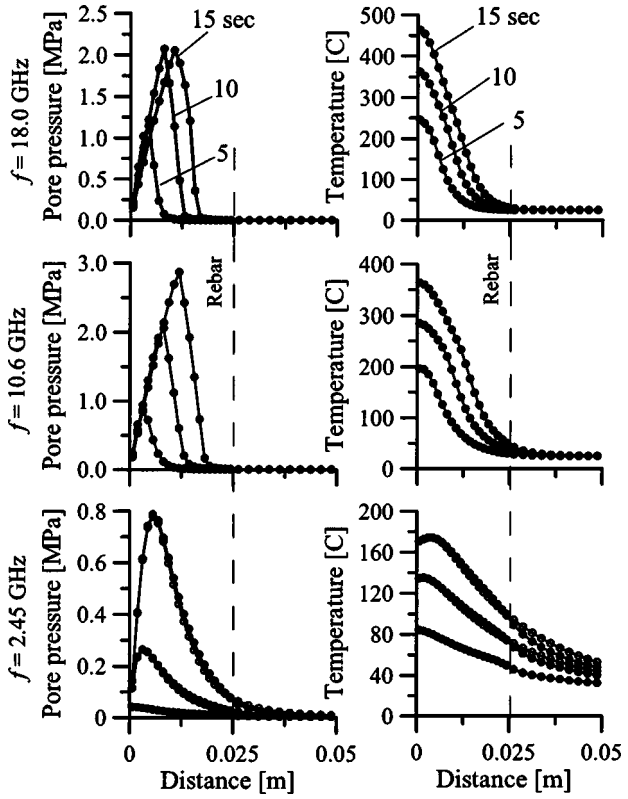

Fig. 4. Effect of different frequencies on pore pressure and temperature profiles; solid dots represent the case with reinforcing bars and circles represent the case without reinforcing bars

surface of the wall) is considered to be about 19%. The location of the bars is marked by the dashed lines in the figure.

The center of the reinforcing bars in concrete structures is located typically at 2.5–4 cm below the surface. At that depth, the electromagnetic power is almost exhausted by the power dissipation (Fig. 2). Therefore, it appears that the existence of steel bars is not important for the decontamination process. However, note that this argument is not true in general. It holds true only for the high-power decontamination process and typical reinforced concrete structures. If much lower frequencies were used or if a conductive material, the steel, were located closer to the concrete surface, this effect could get important.

Effect of Microwave Frequencies on Pore Pressures and Temperatures

The effects of different frequencies, $f=2.45$, 10.6, and 18.0 GHz, are plotted in Fig. 4. The same initial power density, $P_0=1.1\ \mathrm{MW/m^2}$, is considered for every case. As the frequency increases, the location of the peaks of pore pressure and temperature shift toward the heated surface. The reason is that the energy dissipation rate is higher at a higher frequency.

The maximum pore pressure for $f=18.0$ GHz after 10 seconds of heating is $P_{\max,10}=2.0$ MPa at 7.5 mm below the surface. If this pore pressure acted on an unrestrained element of concrete, it would produce in concrete the tensile volumetric (hydrostatic) stress $\sigma_V \approx 0.1\times 2.0=0.2$ MPa, where the value 0.1 is adopted for the typical porosity of concrete. Compared to the tensile strength of ordinary concrete, $f_t' \approx 4$ MPa, this value of tensile volumetric stress is only about 5% of f_t'.

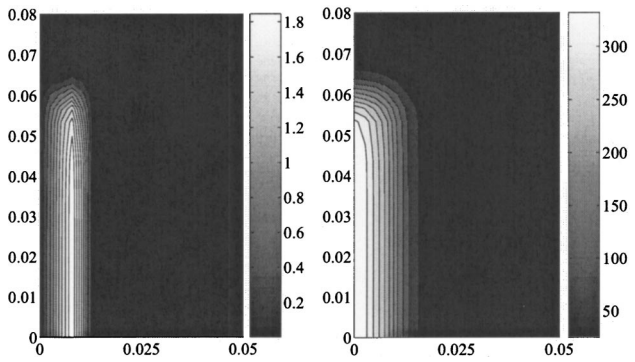

Fig. 5. Contour plot of development of pore pressure (left; MPa) and temperature (right; °C) after 10 heating with $f=18.0$ GHz and $P_0=1.1\ \mathrm{MW/m^2}$

The effect of pore pressure is in fact even weaker since the foregoing estimate is the maximum possible pore pressure if the additional pore space created by the formation of microcracks has been neglected. Taking it into account, an even smaller tensile volumetric stress in an unrestrained element of concrete would be indicated. So, although the effect of pore pressure is not completely negligible, it cannot be the main cause of spalling.

Fig. 5 shows the contour plot of pore pressure and temperature that develops after 10 s of heating at frequency $f=18.0$ GHz and power input $P_0=1.1\ \mathrm{MW/m^2}$. As we can see, the heated zone is localized very near the heated surface.

Stress Fields and Triggering of Spalling

Because the distributed cracking described by the microplane model represents strain softening, the stress and deformation analysis must employ some localization limiter (Bažant 2002), which could have the form of either the crack band model or some of the nonlocal models (Bažant and Ožbolt 1990, 1992; Ožbolt and Bažant 1996; Jirásek and Bažant 2002). The former has been adopted for the present purpose. Thus the finite element size l_c is fixed as a material property. The proper value of l_c depends on the postpeak softening slope of the uniaxial tensile response given by the constitutive model.

The constitutive model gives a good match of material test data when the finite element in the test specimens size is about 5 mm. The same finite element size l_c is, therefore, adopted here, although this is less than the typical maximum aggregate size in concrete. The thickness of the layer that spalls off within about 10 seconds as a result of microwave heating is also about 5 mm, as revealed by experimental trials of microwave induced spalling (White et al. 1995). Unfortunately, the data from these trials cannot be used to verify the present theoretical predictions because the material properties were not documented (not even the compressive strength f_c' of the concrete in the wall subjected to microwave heating was measured). Only the average depth of the removed surface layer was recorded (White et al. 1995). Therefore, the typical properties of concrete used in the nuclear facilities had to be assumed for the present numerical simulations.

Fig. 6 shows the available experimental data (Jansen and Shah 1997) and their numerical fitting using the present theoretical model. Fig. 7 depicts the constant-value contour plots of the computed strain field after 10 s of microwave heating; it shows the mechanical strain, i.e., the total (elastic plus viscoelastic) strain

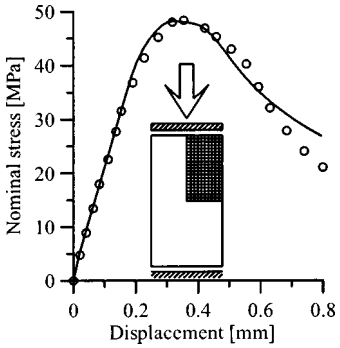

Fig. 6. Uniaxial compression data of 10.17 cm×20.03 cm cylinder tested by Jansen and Shah (1997) (circles) and its optimal fitting (solid line) by finite element simulation in which axisymmetric quadrilateral elements of size 5 mm by 5 mm are used; $E=48.5$ GPa, $k_1=0.000125$, $k_2=160.0$, $k_3=6.4$, and $k_4=150.0$

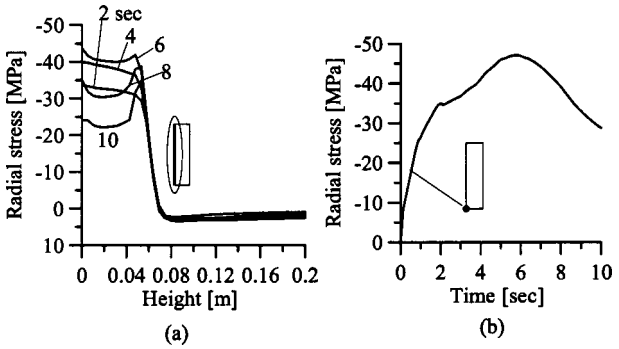

Fig. 8. (a) Distribution of radial stress with respect to height and (b) evolution of radial stress at center of heated zone by time

minus the hygrothermal strain (strain produced by changes of temperature and water content). It is found that the maximum principal mechanical strain in the surface layer exceeds 0.005 in tension and the strain state is essentially biaxial (Fig. 8). This strain value is much higher than the typical strain at peak in uniaxial tension (about 0.0002). It follows that the concrete must undergo postpeak softening and suffer disintegration by cracking. The compressive stress induced by the temperature increase is resisted not only by radial and circumferential biaxial compression generated by the resistance of the cold concrete mass surrounding the heated zone, but also by tensile stress in the circumferential direction of the axisymmetric mesh caused by radial expansion (a situation similar to that analyzed by Ulm et al., 1999).

Is Spalling Triggered by Pore Pressure or Compressive Thermal Stress?

The question of the main cause of spalling of the surface layer of a rapidly heated concrete wall has been the subject of many debates. One school of thought, initiated by Harmathy (1965, 1970), Harmathy and Allen (1973), Li et al. (1993), and Lagos et al. (1995), holds that the pore water cannot escape fast enough (a phenomenon called ''moisture clog'') and thus develops high vapor pressures which cannot be resisted by the tensile strength of concrete. Another school of thought (Bažant 1997) is that the thermal expansion of the saturated heated zone, resisted by the cold concrete mass that surrounds the heating zone, leads in the surface layer to very high compressive stresses parallel to surface which either crush concrete, or cause the compressed surface layer to buckle, or both.

The relative significance of these two mechanisms must of course depend on the type of problem, and can be different for microwave heating in the bulk of concrete and for conductive heating by fire. In the present problem, the highest pore pressure calculated has the value 2.0 MPa, which causes in concrete a hydrostatic tension of about 0.2 MPa. This value is not enough to initiate spalling concrete. Besides, as soon as cracks start to form, the volume available to pore water rapidly increases (by orders of magnitude), which must cause a rapid drop of pore pressure before the cracks can become large and open widely (Bažant 1997).

So it appears that the pore pressure development cannot be the main cause of spalling, although it is not a negligible factor in the triggering of spalling. The main cause must be the compressive stresses along radial lines emanating from the center of the heated zone. These stresses, engendered by the resistance of cold concrete to the thermal expansion of the heated zone, reach values as high as about 50 MPa [Fig. 8(b)], according to the present analysis. This is certainly enough to cause compressive crushing as well as buckling of the compressed layer.

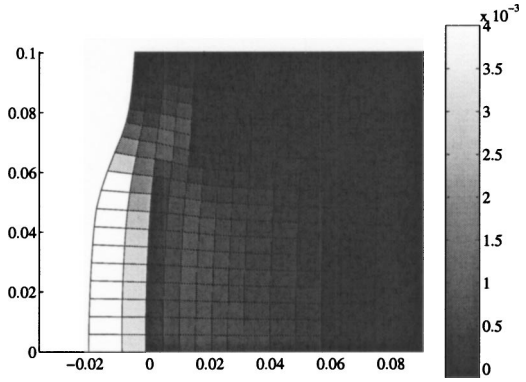

Fig. 7. Contour plot of mechanical strain ε_1 after 10 s heating, in which deformation is exaggerated by 100

Application of Finite Volume Method to Heat and Water Transfer in Concrete

Since the finite volume method (Eymard et al. 1998, 2000) has not been used for the coupled heat and water transfer problems of concrete, its application will now be described. In this method, the domain is divided into discrete control volumes (Fig. 9). The interfaces (or boundaries) of a control volume are placed midway between adjacent representative points (which is generally accomplished by Voronoi tessellation, although that approach is not needed for the regular node arrangement used here). The discretization equations are derived by integrating Eqs. (19) and (20) of Part I over the control volume shown in Fig. 9(a), and over the time interval from t to $t+\Delta t$

$$(w_0^{i+1,m+1}-w_0^i)+c_x(J_e-J_w)^{i+1,m+1}+c_y(J_n-J_s)^{i+1,m+1}=I_{(w)}^{i+1,m+1} \tag{3}$$

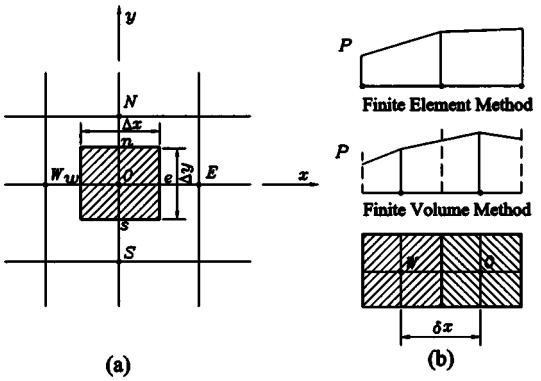

Fig. 9. (a) Two dimensional discretization of finite volume where *W,E,S, N* = labels for West, East, South, and North; shaded rectangle represents control volume and (b) difference in pressure (or temperature) profiles implied by finite element and finite volume methods

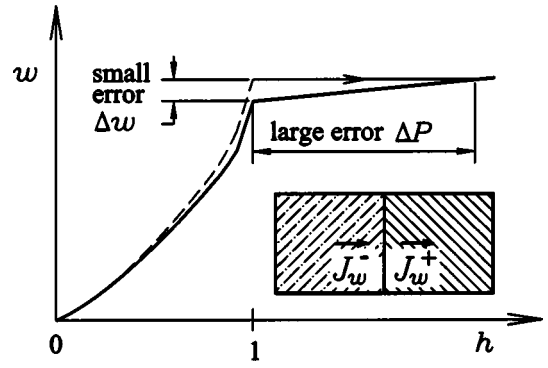

Fig. 10. Explanation why small error in water content caused by lack of exact mass balance can cause enormous error in pore pressure

$$[(\rho C)_0(T_0^{i+1,m+1}-T_0^i)]+c_x(q_e-q_w)^{i+1,m+1}$$
$$+c_y(q_n-q_s)^{i+1,m+1}=I_{(h)}^{i+1,m+1} \tag{4}$$

where i = label for time step ($i=1,2,\ldots$); m = label for iteration number in an implicit scheme ($m=1,2,\ldots$); 0 = label for current control volume [the center point in Fig. 9(a)]; *s,e,n, w* = labels for south, east, north, and west interfaces, respectively, of a square control volume in Fig. 9; $c_x=\Delta t/\Delta x$ and $c_y=\Delta t/\Delta y$ for a two-dimensional plane flow problem; $c_y=\Delta t/y_0\Delta x$ if y is the radial direction in the axisymmetric flow problem, where y_0 is the radial distance of point 0 from the radial center; and Δx, Δy = sizes of the current control volume (Fig. 9). Due to severe nonlinearity of the problem, modified Picard's iteration (Celia et al. 1990), in which the differential coefficients of the fluxes are taken as constants during each iteration, is adopted to solve the partial differential equations.

To calculate the fluxes at the control–volume interfaces, linear distributions of the state variables between the representative points are assumed. This simplifies the calculation of the flux at an interface. For example,

$$J_w=-\frac{a_w}{g}\frac{P_0-P_W}{x_0-x_W} \tag{5}$$

where J_w = water flux through the interface W (west); a_w = interface permeability at interface W; P_0, P_W = pore pressures at points 0 and W (west); and x_0, x_W = distances of the points 0 and W from the center [Fig. 9(a)].

Note that, in the finite volume method, the flux J_w at the west interface of current control volume 0 [Fig. 9(b)] is exactly equal to the flux J_e at the east interface of the adjacent control volume lying to the west, even though the flux values are only approximate. Therefore, the condition of local mass balance (as well the condition of local heat balance) is satisfied in the finite volume method exactly. This is a well-known advantage of the finite volume method, important for avoiding spurious oscillation in highly nonlinear problems with high local gradients and sharp fronts. The advantage of the finite volume method for the analysis of moisture transfer in concrete was recognized already by Eymard et al. (1998) and was explored by Mainguy and Coussy (2000) in the problem of calcium leaching from concrete, although in the absence of heat transfer. Mainguy et al. (2001a) showed an effective application of the finite volume method to drying of porous materials.

In the finite element approach, by contrast, the local mass balance cannot be satisfied exactly. For example, if standard finite elements with linear shape functions are used [Fig. 9(b)], then the flux at the west boundary of the current control volume 0 is generally different from the flux at the east boundary of the adjacent control volume lying to the west [note the different slopes adjoining the interface in Fig. 9(b)]. Nevertheless, for a special case of mass lumping (achieving pressure interpolation imitating the finite volume method), in low-order finite elements and for implicit time integration applied to coupled diffusion–dissolution problems, the finite element method gives the same results as the finite volume method and provides an accurate oscillation-free determination of sharp fronts (Mainguy et al. 2001b).

The reason why exact local mass balance is needed to avoid spurious oscillation of pressure and concentration (water content) is explained by Fig. 10, showing a sharp change of slope of the sorption isotherm of relative pore pressure h (humidity) versus water concentration w (specific pore water content). At the transition from unsaturated to saturated state ($h=1$), a very small error Δw in water concentration, which is insignificant for the pressures in the unsaturated states, is seen to cause an enormous change of pressure in the saturated state (because the slope of the pressure concentration isotherm drops above $h=1$ by orders of magnitude). This means that if the control volume with outflux J_w^- is unsaturated and the adjacent control volume with influx J_w^+ is saturated, even a very small error in J_w^- would cause a very large pressure change in the saturated control volume.

The heat generation $I_{(h)}$ depends on the water contents of all the control volumes along the wave propagation path. The water contents, in turn, depend on the pore pressures and temperatures produced by the microwave heating. To avoid the complication that stems from this mutual coupling, the heat generation $I_{(h)}$ is in each time step calculated explicitly, based on the water contents of the control volumes in the last previous time step. The error caused by this one-step delay in the calculation of heat generation is very small if a small time step is used.

After taking the first-order Taylor expansion of the terms superscripted by $m+1$ and collecting the terms that contain the variations δP and δT from one iteration to the next (in the same time step), one obtains the following system of algebraic linear equations:

$$K_{P_0}^M\delta P_0+K_{P_W}^M\delta P_W+K_{P_S}^M\delta P_S+K_{P_E}^M\delta P_E+K_{P_N}^M\delta P_N+K_{T_0}^M\delta T_0$$
$$+K_{T_W}^M\delta T_W+K_{T_S}^M\delta T_S+K_{T_E}^M\delta T_E+K_{T_N}^M\delta T_N=R^M \tag{6}$$

$$K^H_{P_0}\delta P_0+K^H_{P_W}\delta P_W+K^H_{P_S}\delta P_S+K^H_{P_E}\delta P_E+K^H_{P_N}\delta P_N+K^H_{T_0}\delta T_0$$
$$+K^H_{T_W}\delta T_W+K^H_{T_S}\delta T_S+K^H_{T_E}\delta T_E+K^H_{T_N}\delta T_N=R^H \quad (7)$$

where

$$K^M_{P_0}=c_x(a^{i+1,m}_w/\delta x_w)+c_y(a^{i+1,m}_s/\delta x_s)+c_x(a^{i+1,m}_e/\delta x_e)$$
$$+c_y(a^{i+1,m}_n/\delta x_n) \quad (8)$$

$$K^M_{P_W}=-c_x(a^{i+1,m}_w/\delta x_w),$$
$$K^M_{P_S}=-c_y(a^{i+1,m}_s/\delta x_s), \quad (9)$$
$$K^M_{P_E}=-c_x(a^{i+1,m}_e/\delta x_e),$$
$$K^M_{P_N}=-c_y(a^{i+1,m}_n/\delta x_n) \quad (10)$$

$$K^M_{T_0}=(\partial w/\partial T)^{i+1,m}-(\partial I_{(w)}/\partial T)^{i+1,m},$$
$$K^M_{T_W}=K^M_{T_S}=K^M_{T_E}=K^M_{T_N}=0 \quad (11)$$

$$R^M=-[(w^{i+1,m}_0-w^i_0)+c_x(J_e-J_w)^{i+1,m}$$
$$+c_y(J_n-J_s)^{i+1,m}-I^{i+1,m}_{(w)}] \quad (12)$$

$$K^H_{P_0}=K^H_{P_W}=K^H_{P_S}=K^H_{P_E}=K^H_{P_N}=0 \quad (13)$$

$$K^H_{T_0}=\rho C \quad (14)$$

$$K^H_{T_W}=-c_x(k^{i+1,m}_w/\delta x_w),$$
$$K^H_{T_S}=-c_y(k^{i+1,m}_s/\delta x_s), \quad (15)$$
$$K^H_{T_E}=-c_x(k^{i+1,m}_e/\delta x_e),$$
$$K^H_{T_N}=-c_y(k^{i+1,m}_n/\delta x_n) \quad (16)$$

$$R^H=-[\rho CT^{i+1,m}+c_x(q_e-q_w)^{i+1,m}+c_y(q_n-q_s)^{i+1,m}-I_{(h)}] \quad (17)$$

Here δx, δy = distances between the representative points of adjacent control volumes [Fig. 9(b)]; M = label for mass; H = label for heat; R = residual which is to be reduced to almost zero by the iteration; S,E,N, W = labels for control volumes adjacent to the current control volume 0 in the direction of south, east, north, and west, respectively, in Fig. 9(a); a = interface permeability; and k = interface heat conductivity.

The differential coefficients of the fluxes need to be multiplied by the radial distance of the corresponding interfaces if an axisymmetric problem is considered. The interface permeability is easily computed from the mass conservation condition. For example, if a steady state flow is considered, the mass flux on the interface w measured with respect to west control volume must be equal to the mass flux measured with respect to the current control volume 0 [see Fig. 9(a)]. Therefore, the equivalent permeability of the interface is

$$a_w=\frac{a_W a_0}{fa_W+(1-f)a_0} \quad (18)$$

where f = constant representing the location of interface; a_W = representative permeability of west control volume; and a_0 = representative permeability of current control volume. The interface heat conductivity is calculated by Eq. (18) similarly. One can calculate the interface permeability at boundaries from Eq. (18), too. For example, when the surface emissivity is infinite, the interface permeability of the west boundary surface is $a=a_0$.

Conclusions

1. The computations confirm that the power and efficiency of the microwave applicator is a key factor for the proposed decontamination process. For the maximum power efficiency considered, the heat generation per unit volume of the wall is almost three times greater than it is for zero efficiency. Therefore the efficiency should be accurately measured.
2. In view of the high microwave frequencies considered, averaging of the heating rate over the spatial wavelength and the time period causes no appreciable error.
3. The calculations confirm that a 5 mm thick surface layer of typical concrete can be spalled off within 10 s of microwave heating of frequency 18.0 GHz and power 1.1 MW/m^2.
4. Calculations show that the thickness of the concrete wall has a negligible effect on the evolution of pore pressure and temperature. The reason is the short heating duration which is of the order of 10 s only. For long heating durations, differences would of course be obtained, due to microwave reflection and heat loss at the opposite surface of wall.
5. The electromagnetic power carried by the microwaves is almost exhausted when the waves reach the location of the reinforcing bars in typical concrete structures. Therefore, the same decontamination process can be used for both unreinforced and reinforced concrete walls.
6. The pore water pressure caused by heating is not negligible but is not a major factor. The main cause of spalling is high compressive stress parallel to surface along the radial lines emanating from the heated zone and high tensile stress along the circumferential lines, both produced by thermal expansion of the heated zone confined by cold concrete.
7. The present computational experience confirms that the finite volume method is preferable to the finite element method for simultaneous heat and mass transfer in concrete heated to high temperature. Adoption of this method helps to eliminate spurious oscillations of response caused by propagation of a sharp interface with order-of-magnitude jumps in pore pressure and permeability (the interface separates a saturated zone from a nonsaturated zone, or a cold zone of small permeability from a hot zone of a high permeability).

Acknowledgments

Grateful appreciation is due to the Department of Energy for supporting both parts of this study under Grant No. DE-FG07-98ER45736 to Northwestern University. Thanks are due to Dr. Brian Spalding of the Oak Ridge National Laboratory for valuable consultations and constructive monitoring of the progress of this research.

Appendix I: Input Data for Analysis

The input data for the parametric studies of microwave heating in Figs. 3, 4, 5, and 11 are as follows: age of concrete = 20 years; initial relative humidity in the pores $h_0=0.6$; $T_0=25.0°C$; saturation water content = 135 kg/m^3; apparent mass density of concrete = 2288 kg/m^3; heat capacity of concrete = 1000 J/kg °K; reference permeability = 40.5×10^{-12} m/s; heat conductivity

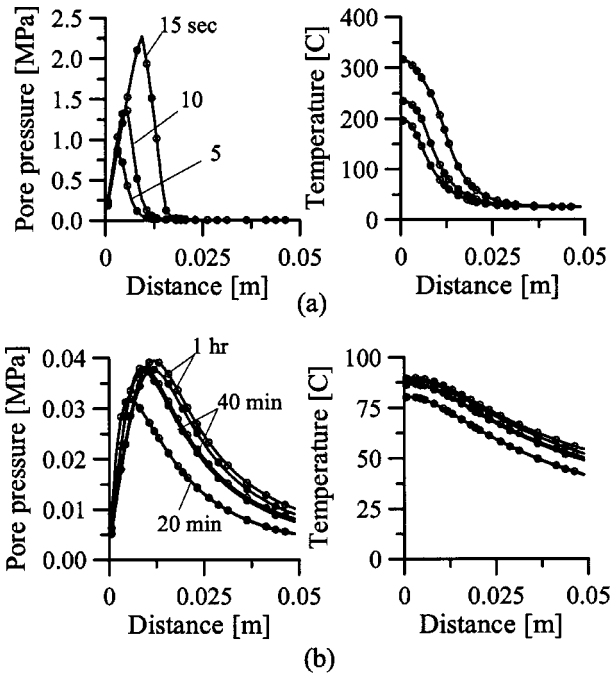

Fig. 11. Effect of wall thickness on pore pressure and temperature profiles in which $f=10.6$ GHz is used; (top) rapid heating with high power (1.1 MW/m^2); (bottom) slow heating with low power (0.01 MW/m^2). Solid dots represent profiles across 30 cm wall and circles represent profiles across 10 cm wall.

$=3.67$ J/m^2 s °C; amount of unhydrous cement$=227$ kg/m^3; mass transfer coefficient of water flux$=\infty$; heat transfer coefficient of heat flux$=10.0$ J/m^2 s °C; relative dielectric permittivity ϵ'/ϵ_0 of concrete$=5.0$; surface emissivity$=0.9$; the range of frequencies applied$=2.45-18.0$ GHz; the initial power density $=1.1$ MW/m^2 for the rapid heating and 0.011 MW/m^2 for the slow heating; the area fraction of reinforcing bars in a plane parallel to surface$=19\%$; distance of the centroid of reinforcing bars from concrete surface$=$ at least 2.5 cm.

The input data for the mechanical deformation analysis are: $E=48.5$ GPa; $k_1=0.000125$, $k_2=160$, $k_3=6.4$, and $k_4=150.0$ for the microplane model; the thermal expansion coefficient $=\alpha_T=12.0\times10^{-6}$.

Appendix II: Effect of Wall Thickness on Pore Pressures and Temperatures

Fig. 11(a) shows the pore pressure and temperature profiles for two different wall thicknesses, 10 and 30 cm, after 5, 10, and 15 s of heating with the power density $P_0=1.1$ MW/m^2, which is quite high and equals the power intensity used by White et al. (1995). For the short durations (about 10 s), contemplated for the decontamination process, the profiles obtained for two different wall thicknesses are almost identical (White et al. 1995) (and doubtless also about the same as in a half space).

If the wall were heated for a relatively long time with a low power density, appreciable differences in the temperature profiles would be observed because of the power reflected from the wall surface opposite to the heated surface; see Fig. 11(b); $P_0=0.01$ MW/m^2. A wall 10 cm thick would be heated a little faster than a wall 30 cm thick. But the differences are still very small.

Appendix III: Review of Microplane Constitutive Model for Concrete

For readers's convenience, model M4, already mentioned and referenced to in Part I will now be summarized (Bažant et al. 2000; Caner and Bažant 2000). The strain vectors on the plane of any orientation within the material, called the microplane, are assumed to be the projections of the continuum (macroscopic) strain tensor ε_{ij} (where the subscripts, $i=1,2,3$ refer to Cartesian coordinates x_i). This is called the kinematic constraint. Thus the component of the strain vector ε_j^n on any microplane is $\varepsilon_j^n=\varepsilon_{jk}n_k$ (Bažant and Prat 1988) where n_i are the direction cosines of the normal to the microplane. The normal strain vector is $\varepsilon_{N_i}=n_in_jn_k\varepsilon_{jk}$, and its magnitude is $\varepsilon_N=n_j\varepsilon_j^n=n_jn_k\varepsilon_{jk}=N_{ij}\varepsilon_{ij}$, where $N_{ij}=n_in_j$ (the repeated Latin lowercase subscripts indicate summation over 1, 2, 3). The magnitude of the strain vector on the microplane is $\|\varepsilon_j^n\|=\sqrt{\varepsilon_j^n\varepsilon_j^n}$. The shear strain components in two orthogonal (suitably chosen) directions m_i and l_i tangential to the microplane (normal to n_i) are $\varepsilon_M=m_i(\varepsilon_{ij}n_j)$ and $\varepsilon_L=l_i(\varepsilon_{ij}n_j)$. Because of the symmetry of ε_{ij}, $\varepsilon_M=M_{ij}\varepsilon_{ij}$, $\varepsilon_L=L_{ij}\varepsilon_{ij}$, where $M_{ij}=(m_in_j+m_jn_i)/2$ and $L_{ij}=(l_in_j+l_jn_i)/2$ (Bažant and Prat 1988).

Since the kinematic constraint relates the strains on the microplanes to the macroscopic strain tensor, the static equivalence can be enforced only approximately. This is done by means of the virtual work theorem which is written for the surface of a unit hemisphere (Bažant 1984)

$$\frac{2\pi}{3}\sigma_{ij}\delta\varepsilon_{ij}=\int_\Omega(\sigma_N\delta\varepsilon_N+\sigma_L\delta\varepsilon_L+\sigma_M\delta\varepsilon_M)\mathrm{d}\Omega \tag{19}$$

$$=\int_\Omega(\sigma_NN_{ij}+\sigma_LL_{ij}+\sigma_MM_{ij})\delta\varepsilon_{ij}\mathrm{d}\Omega \tag{20}$$

The normal stress and normal strain are split into their volumetric and deviatoric parts, and if Eq. (20) is written separately for the volumetric and deviatoric components, one has

$$\sigma_{ij}=\sigma_V\delta_{ij}+\sigma_{ij}^D \tag{21}$$

$$\sigma_{ij}^D=\frac{3}{2\pi}\int_\Omega\left[\sigma_D\left(N_{ij}-\frac{\delta_{ij}}{3}\right)+\sigma_LL_{ij}+\sigma_MM_{ij}\right]\mathrm{d}\Omega \tag{22}$$

The elastic increments of the stresses in each microplane over the time step (or load step) are written as $\Delta\sigma_V=E_V\Delta\varepsilon_V$, $\Delta\sigma_D=E_D\Delta\varepsilon_D$, and $\Delta\sigma_T=E_T\Delta\varepsilon_T$, where $E_V=E/(1-2\nu)$; $E_D=5E/(2+3\eta)(1+\nu)$, and $E_T=\eta E_D$. Here η is a parameter that can be chosen; the best choice is $\eta=1$ (Carol et al. 1991; Bažant et al. 1996; Carol and Bažant 1997). The volumetric–deviatoric split makes it possible to reproduce the full range of Poisson ratio $-1\leqslant\nu\leqslant0.5$ in elastic analysis. The term $-\delta_{ij}/3$ in Eq. (22) ensures that $\sigma_{kk}^D=0$ even when $\int_\Omega\sigma_D\mathrm{d}\Omega\neq0$.

The integration is conducted numerically according to an optimal Gaussian quadrature integration formula for a spherical surface, characterized by discrete directions μ and associated weights w_μ; $\sigma_{ij}=(3/2\pi)s_{ij}\approx6\Sigma_{\mu=1}^Nw_\mu s_{ij}^{(\mu)}$, where $s_{ij}=\int_\Omega(\sigma_NN_{ij}+\sigma_LL_{ij}+\sigma_MM_{ij})\delta\varepsilon_{ij}\mathrm{d}\Omega$ and $N=$ the number of the microplanes.

The inelastic behavior with fracturing damage, modeled as strain softening, is characterized on the microplanes in terms of strain-dependent yield limits for the components σ_V, σ_D, σ_N, σ_L and σ_M, called the stress–strain boundaries. These boundaries can approximately reflect various physical mechanisms such as frictional slip in a certain direction, progressive growth of micro-

cracks of a certain orientation, axial splitting, lateral spreading under compression, etc.

The constitutive model is explicit. In each time step, and at each integration point of each finite element, the newly calculated strain tensor is supplied as the input to the microplane constitutive subroutine. From this, the subroutine first calculates the strain components on all the discrete microplanes (whose number, from experience, must be at least 21, for acceptable accuracy). From those components, the stresses are calculated first elastically, and if any stress component exceeds the value on the stress–strain boundary for the given strain, the stress value is dropped onto the boundary at constant strain. From the stresses on the microplane, the continuum stress tensor is calculated as the output, which is then used by the finite element program to calculate the nodal forces.

References

Ahmed, G. N., and Hurst, J. P. (1997). ''Coupled heat and mass transport phenomena in siliceous aggregate concrete slabs subjected to fire.'' *Fire Mater.,* 21, 161–168.

Bažant, Z. P. (1984). ''Microplane model for strain controlled inelastic behavior.'' *Mechanics of engineering materials,* C. S. Desai and R. H. Gallagher, eds., Chap. 3, Wiley, London, 45–59.

Bažant, Z. P. (1997). ''Analysis of pore pressure, thermal stress and fracture in rapidly heated concrete.'' *Proc., Int. Workshop on Fire Performance of High-Strength Concrete*, NIST Special Publication 919, L. T. Phan et al., eds., National Institute of Standards and Technology, Gaithersburg, Md., 155–164.

Bažant, Z. P. (2002). *Scaling of structural strength*, Hermes-Penton, London.

Bažant, Z. P., Caner, F. C., Carol, I., Adley, M. D., and Akers, S. A. (2000). ''Microplane model M4 for concrete I: Formulation with work-conjugate deviatoric stress.'' *J. Eng. Mech.,* 126(9), 944–953.

Bažant, Z. P., and Kaplan, M. F. (1996). *Concrete at high temperatures*, Longman, London.

Bažant, Z. P., and Ožbolt, J. (1990). ''Nonlocal microplane model for fracture, damage and size effect in structures.'' *J. Eng. Mech.,* 116(11), 2484–2504.

Bažant, Z. P., and Ožbolt, J. (1992). ''Compression failure of quasi-brittle material: Nonlocal microplane model.'' *J. Eng. Mech.,* 118(3), 540–556.

Bažant, Z. P., and Prat, P. C. (1988). ''Microplane model for brittle plastic material: I. Theory.'' *J. Eng. Mech.,* 114(10), 1672–1688.

Bažant, Z. P., and Thonguthai, W. (1978). ''Pore pressure and drying of concrete at high temperature.'' *J. Eng. Mech. Div., Am. Soc. Civ. Eng.,* 104(5), 1059–1079.

Bažant, Z. P., and Thonguthai, W. (1979). ''Pore pressure in heated concrete walls: Theoretical prediction.'' *Mag. Concrete Res.,* 31(107), 67–76.

Bažant, Z. P., Xiang, Y., and Prat, P. C. (1996). ''Microplane model for concrete. I. Stress–strain boundaries and finite strain.'' *J. Eng. Mech.,* 122(3), 245–254; 123(3), E411–E411.

Bažant, Z. P., and Zi, G. (2003). ''Decontamination of radionuclides from concrete by microwave heating. I: Theory.'' *J. Eng. Mech.,* 129(7), 777–784.

Caner, F. C., and Bažant, Z. P. (2000). ''Microplane model M4 for concrete II: Algorithm and calibration.'' *J. Eng. Mech.,* 126(9), 954–961.

Carol, I., and Bažant, Z. P. (1997). ''Damage and plasticity in microplane theory.'' *Int. J. Solids Struct.,* 34(29), 3807–3835.

Carol, I., Bažant, Z. P., and Prat, P. C. (1991). ''Geometric damage tensor based on microplane model.'' *J. Eng. Mech.,* 117(10), 2429–2448.

Celia, M. A., Bouloutas, E. T., and Zarba, R. L. (1990). ''A general mass-conservative numerical solution for the unsaturated flow equation.'' *Water Resour. Res.,* 26(7), 1483–1496.

Cheng, D. K. (1983). *Field and wave electromagnetics*, Addison–Wesley, London.

Eymard, R., Gallouët, T., and Herbin, R. (2000). ''The fine volume methods.'' *Handbook of numerical analysis*, P. G. Ciarbet and J. L. Lions, eds., North Holland, Amsterdam.

Eymard, R., Gallouët, T., Hilhorst, D., and Slimane, Y. N. (1998). ''Finite volumes and nonlinear diffusion equations.'' *RAIRO-Mathematical Modelling and Numerical Analysis—Modélisation Mathématique et Analyse Numérique,* 32(6), 747–761.

Harmathy, T. Z. (1965). ''Effect of moisture on the fire endurance of building materials.'' *Moisture in Materials in Relation to Fire Tests. ASTM Special Technical Publication No. 385*, American Society of Testing Materials, Philadelphia, 74–95.

Harmathy, T. Z. (1970). ''Thermal properties of concrete at elevated temperatures.'' *J. Mater.,* 5(1), 47–74.

Harmathy, T. Z., and Allen, L. W. (1973). ''Thermal properties of selected masonry unit concrete.'' *ACI J.,* 70(2), 132–142.

Jansen, D. C., and Shah, S. P. (1997). ''Effect of length on compressive strain softening of concrete.'' *J. Eng. Mech.,* 123(1), 25–35.

Jirásek, M., and Bažant, Z. P. (2002). *Inelastic analysis of structures*, Vol. 735, Wiley, London.

Kraus, J. D. (1988). *Antennas*, MacGraw–Hill, New York.

Lagos, L. E., Li, W., and Ebadian, M. A. (1995). ''Heat transfer within a concrete slab with a finite microwave heating source.'' *Int. J. Heat Mass Transf.,* 38(5), 887–897.

Li, W., Ebadian, M. A., White, T. L., and Grubb, R. G. (1993). ''Heat transfer within a concrete slab applying the microwave decontamination process.'' *J. Heat Transf.,* 115, 42–50.

Mainguy, M., and Coussy, O. (2000). ''Propagation fronts during calcium leaching and chloride penetration.'' *J. Eng. Mech.,* 126(3), 250–257.

Mainguy, M., Coussy, O., and Baroghel-Bouny, V. (2001a). ''Role of air pressure in drying of weakly permeable materials.'' *J. Eng. Mech.,* 127(6), 582–592.

Mainguy, M., Ulm, F.-J., and Heukamp, F. H. (2001b). ''Similarity properties of demineralization and degration of cracked porous materials.'' *Int. J. Solids Struct.,* 38, 7079–7100.

Ožbolt, J., and Bažant, Z. P. (1996). ''Numerical smeared fracture analysis: Nonlocal microcrack interaction approach.'' *Int. J. Numer. Methods Eng.,* 39, 635–661.

Patankar, S. V. (1980). *Numerical heat transfer and fluid mechanics*, McGraw–Hill, New York.

Ulm, F.-J., Coussy, O., and Bažant, Z. P. (1999). ''The ''Chunnel'' fire. I: Chemoplastic softening in rapidly heated concrete.'' *J. Eng. Mech.,* 125(3), 272–282.

White, T. L., Foster, D., Jr., Wilson, C. T., and Schaich, C. R. (1995). ''Phase II microwave concrete decontamination results,'' *ORNL Rep. No. DE-AC05-84OR21400*, Oak Ridge National Laboratory, Oak Ridge, Tenn.